Check for updates

MATERIALS SCIENCE

Electrostriction-driven phase instability enables giant pseudo-piezoelectricity in $Hf_{0.5}Zr_{0.5}O_2$

Achilles Bergne[1], Milica Vasiljevic[1]*, Denis Alikin[2], Victor Buratto Tinti[1], Leonardo Oliveira[3,4], Megan O. Landberg Hill[4], Huaiyu Chen[4], Jesper Wallentin[3], Dylan Jennings[5,6,7,8], Wolfgang Rheinheimer[5], Henrik Bruus[9], Mathias Grønborg[9], Dimitrios Koukoulis[1], Armando Antonio Morin-Martinez[1], Javier Zamudio-García[1], Ivano Eligio Castelli[1], Reinis Ignatāns[10], Andrei Kholkin[2,10], Dennis Valbjørn Christensen[1,11], Nini Pryds[1], Vincenzo Esposito[1]*

Copyright © 2026 The Authors, some rights reserved; exclusive licensee American Association for the Advancement of Science. No claim to original U.S. Government Works. Distributed under a Creative Commons Attribution NonCommercial License 4.0 (CC BY-NC).

The electromechanical properties of hafnium zirconium oxide fluorite ($Hf_{0.5}Zr_{0.5}O_2$, HZO) remain largely unexplored despite its widespread use as a ferroelectric in CMOS-compatible devices. Here, we demonstrate that electrostriction-driven phase instability enables a giant pseudo-piezoelectric response in epitaxial HZO thin films. Above a critical field of 24 kilovolts per centimeter, field-induced transitions between nonpolar and polar phases activate an extrinsic piezoelectric response of ~1000 picometers per volt and bias-stabilized pseudo-piezoelectric strains exceeding 10,000 picometers per volt. This behavior arises from a combination of large electrostriction ($M = 1 \times 10^{-14}$ square meters per square volt), ferroelastic softness, and structural reconfiguration, rather than intrinsic polarization switching. Multimodal characterization combining interferometry, diffraction methods, scanning probe microscopy, and first-principles modeling confirms the coupling between strain and metastable phase dynamics. These findings reveal a previously unrecognized mechanism for functional strain generation in fluorite oxides, positioning HZO as a versatile platform for strain-engineered actuators, adaptive metasurfaces, and reconfigurable nanoelectromechanical systems.

INTRODUCTION

Electromechanically active thin films are essential in micro- and nanoelectromechanical systems (MEMS and NEMS), where they function as actuators, sensors, and transducers (*1*, *2*). Perovskite oxides such as lead zirconate titanate (PZT) and barium titanate (BTO) (*3*, *4*) dominate these applications but are poorly suited for silicon integration due to chemical instability, structural mismatch, and strict crystallinity requirements (*3*).

Binary metal oxides are emerging as viable alternatives for next-generation electronics due to their simpler chemistry (*5*–*8*). Among these, hafnia (HfO_2) has attracted particular interest for its ferroelectricity in polar fluorite symmetries, as found in Si-doped HfO_2 and $Hf_{0.5}Zr_{0.5}O_2$ (HZO) thin films (*9*–*12*). Already used as high-k dielectrics, hafnia-based films are complementary metal-oxide semiconductor (CMOS) compatible, making them attractive for ferroelectric devices such as memristors, Fe-FETs, tunneling junctions (*4*, *13*–*16*), and MEMS/NEMS devices (*17*).

Although the centrosymmetric monoclinic ($P2_1/c$) phase of HfO_2 is thermodynamically stable (dielectric constant of ~19 to 25) (*18*), doping (*10*, *19*, *20*), defect engineering (*21*), epitaxial strain (*22*–*24*), and electrode or substrate selection (*25*, *26*) can stabilize the metastable orthorhombic ($Pca2_1$) ferroelectric phase. This leads to unconventional ferroelectricity that strengthens with decreasing thickness (*27*, *28*). While HZO's ferroelectricity is well studied (*28*), its electromechanical coupling and piezoelectric behavior remain largely unresolved (*29*–*33*).

Oxygen vacancies are often implicated in modulating HZO's ferroelectric and piezoelectric properties (*34*, *35*). However, Hf^{4+} and Zr^{4+} are isovalent, and their solid solutions do not inherently support charge-compensating oxygen vacancies. Their ionic radii differ only slightly (0.83 Å for Hf and 0.84 Å for Zr), inducing minimal structural distortion. However, their distinct electronic configurations (Hf^{4+}:$4f^{14}$ versus Zr^{4+}:$4p^6$) influence how oxygen vacancies and strain stabilize different polymorphs. In defective fluorite lattices, vacancies permit cation off-centering and enhance local polarizability, with the smaller Hf^{4+} radius altering how metastable polar and nonpolar phases are accessed. Thus, the electromechanical response arises from defect-mediated phase stability rather than intrinsic cation polarizability. Combined with HfO_2's polymorphic landscape, featuring many energetically competitive polar and nonpolar phases, this gives rise to a natural nanoscale metastability (*35*, *36*).

This interplay of structure, polarizability, and metastability parallels recent insights from other electromechanically active fluorite oxides. In ZrO_2, metastable tetragonal phases exhibit antiferroelectricity via stress-driven martensitic transitions (*10*, *37*). In CeO_2-based systems, electrostriction coefficients in the range 10^{-16} to 10^{-14} m^2 V^{-2} have been linked to defect-induced strain fields (*38*–*40*), anharmonic lattice dynamics, and reorientation of elastic dipoles (*41*, *42*). Particularly, Gd-doped CeO_2 shows pseudo-piezoelectric behavior

[1]Department of Energy Conversion and Storage, Denmark Technical University, Lyngby, Denmark. [2]CICECO Aveiro Institute of Materials, Physics Department, Campus de Santiago, University of Aveiro, 3810-193 Aveiro, Portugal. [3]Synchrotron Radiation Research and NanoLund, Lund University, Box 118, Lund 22100, Sweden. [4]MAX IV Laboratory, Lund University, 22100 Lund, Sweden. [5]Institute for Ceramic Materials and Technologies (IKMT), University of Stuttgart, 70569 Stuttgart, Germany. [6]Institute for Energy Materials and Devices, Materials Synthesis and Processing (IMD-2), Forschungszentrum Juelich, 52428 Juelich, Germany. [7]Ernst Ruska-Centre for Microscopy and Spectroscopy with Electrons, Materials Science and Technology (ER-C-2), Forschungszentrum Juelich, 52428 Juelich, Germany. [8]Faculty of Physics and Astronomy, Advanced Transmission Electron Microscopy, Ruhr University Bochum, 44801 Bochum, Germany. [9]Department of Physics, Technical University of Denmark, Fysikvej B309, 2800 Kongens Lyngby, Denmark. [10]Institute of Solid State Physics, University of Latvia, Kengaraga Str. 8, Riga, LV-1063, Latvia. [11]Institute for Advanced Study, Technical University of Munich, Lichtenbergstrasse 2a, D-85748 Garching, Germany.
*Corresponding author. Email: mivas@dtu.dk (M.V.); vies@dtu.dk (V.E.)

Downloaded from https://www.science.org at Forschungszentrum Juelich Gmbh on November 19, 2026

driven by field-induced oxygen vacancy rearrangement, reaching effective coefficients above 1000 pm V^{-1} (*43*). Despite these advances, the electromechanical response of hafnia-based fluorites remains poorly understood, marking a critical gap in how structure, composition, and defect chemistry define functionality in this important class of materials.

In this work, we reveal a previously unrecognized extrinsic electromechanical mechanism in HZO, where field-induced electrostriction drives a reversible transition to a polar phase. This activates a pseudo-piezoelectric response exceeding 10,000 pm V^{-1}, outperforming the best lead-free ceramics. Through compositionally tuned epitaxial films and multimodal characterization, we identify symmetry-breaking phase instability as a design principle for strain engineering in fluorite oxides, with zirconium playing a central role.

RESULTS

Structural characterization and electromechanical response

Epitaxial HZO films are commonly grown on perovskite oxide substrates such as $SrTiO_3$ (STO) (*25*) and (La,Sr)$MnO_{3-\delta}$ (LSMO) (*23*–*25*, *30*, *35*) to stabilize the orthorhombic phase through strain engineering. In this work, we expand this approach by comparing perovskite substrates with fluorite-type single crystals, specifically yttrium-stabilized zirconia (YSZ). YSZ offers a closer lattice match to HZO (5.14 Å versus 5.0 to 5.2 Å), in contrast to the more strained interface imposed by STO (3.905 Å), thus enabling epitaxial growth with reduced structural and microstructural disorder (*44*–*46*).

Figure 1 summarizes the structural, microstructural, and electromechanical properties of HZO and pure hafnia films deposited on both YSZ and STO substrates. On YSZ, the films grow epitaxially with a (100) orientation (see fig. S1), where the monoclinic unit cell aligns the *a* and *b* axes with the in-plane directions of the substrate. The *c* axis is slightly tilted with respect to the out-of-plane direction, as shown in Fig. 1 (A and B), a consequence of the interfacial orientation preference. Scanning transmission electron microscopy (STEM) analysis, including high-angle annular dark-field (HAADF) imaging and selected-area electron diffraction (SAED), confirms the presence of the monoclinic phase in HZO/YSZ films (fig. S2). The close lattice match between HZO and YSZ also suggests a high degree of coherency at the interface. Following phase identification via transmission electron microscopy (TEM), local reciprocal space maps (RSMs) centered near the YSZ (022) reflection reveal that the monoclinic domains are distributed across several orientations, specifically 202, 022, and 02-2, highlighted in Fig. 1 (A and B).

The structural alignment of HZO/STO is more complex due to the larger lattice mismatch, which leads to a rotation of the HZO structure. TEM measurements show that HZO on STO grows in textured columns, with the (011) direction of HZO aligned close to the growth direction. SAED patterns match the orthorhombic HZO phase, while STEM analysis reveals a mix of orthorhombic and monoclinic phases (Fig. 1C and fig. S2). RSMs confirm the coexistence of monoclinic and orthorhombic phases with various orientations. As seen in Fig. 1C, a faint HZO (002) peak is observed near the STO (011) peak, confirming orientations close to (111) for orthorhombic and (11-1) for monoclinic phases. The tetragonal phase does not appear in our characterization, but because of the structural similarities with the orthorhombic phase, we cannot exclude the possibility of local tetragonal domains in highly distorted regions. Further structural details are shown in figs. S1 and S2.

The overall electromechanical coupling of the films is measured using laser interferometry. As shown in Fig. 1D, when a 5-Hz alternating electric field is applied to the lateral electrodes, an induced electromechanical displacement occurs in the vertical direction, which is used to extract the strain and stress of the films as described in Materials and Methods. The experimental strain response shown in Fig. 1D includes first- and second-order harmonics at 5 and 10 Hz, respectively. The overall electromechanical response is the combination of two distinct mechanisms occurring at different frequencies. The inverse piezoelectric effect is a first-order effect and responds with the same frequency as the applied electric field. While electrostriction is a second-order effect and responds at twice the frequency of the applied electric field. The HZO films exhibit a remarkable combination of first- and second-order responses, as the second-order response is higher than the first order.

The second-order electromechanical responses show a quadratic stress increase with the applied alternating electric field, which is characteristic of an electrostrictive response (Fig. 1E). A notable difference between the samples is observed: Unlike hafnia/YSZ, which exhibits no substantial electromechanical response, the HZO samples are exceptionally active electrostrictors. The quadratic response is similar for the HZO/YSZ and the HZO/STO samples, reaching extremely large stress values corresponding to approximately $M_{xx} = 1 \times 10^{-14}$ m^2 V^{-2}, along the *x*-Cartesian axis. As expected, the quadratic electrostrictive response is symmetric as a function of bias.

As with the second-order measurements, the first-order response shows that hafnia/YSZ samples are electromechanically inactive (Fig. 1E, top). All the HZO samples display a similar behavior where the electromechanical stress is minimal at low electric fields, but the first-order "activation" occurs above an electric field threshold of 24 kV cm^{-1}, whereby the first-order response is greatly enhanced. Above this activation threshold, the measured stress varies linearly with the applied electric field.

Figure 1F places our results within the broader landscape of electromechanical responses observed in single-layer ferroelectric and defect-mediated systems in the 1- to 100-Hz range. While the underlying mechanisms may differ, the second-order response of our devices is comparable to the highest-performing thin-film electrostrictors [multilayer CGO and amorphous BTO (*39*, *47*)] and one order of magnitude higher than other materials (*48*–*56*). On both YSZ and STO substrates, the magnitude of M_{xx} drops for films thicker than 10 nm but remains above 2×10^{-16} m^2 V^{-2} for films up to 100-nm thick. The thickness dependence observed in HZO is consistent with earlier findings in CeO_2 and reflects the gradual and reproducible thickness scaling of oxygen-defective fluorite oxides. The first-order response, however, remains low at electric fields below the activation threshold of 24 kV cm^{-1}. The activation is reversible, reproducible on all the samples, repeatable (10 cycles are shown in fig. S3), and does not depend on the thicknesses of the films used in this work (10 to 100 nm). However, increasing the applied voltage could stimulate partial "pinning" of the polar phase, as reported in (*36*, *57*), suggesting that the response may not remain fully reversible at higher fields. After activation, the measured effective piezoelectric coefficient sharply increases to 1000 to 10,000 pm V^{-1}. These effective piezoelectric coefficients after activation are superior to the highest values reported for bulk piezoceramics and relaxors (see Fig. 1F) (*48*–*56*).

Different electromechanical responses of hafnia and HZO films on YSZ, despite their structural similarity, along with crystallographic

Downloaded from https://www.science.org at Forschungszentrum Juelich Gmbh on November 19, 2026

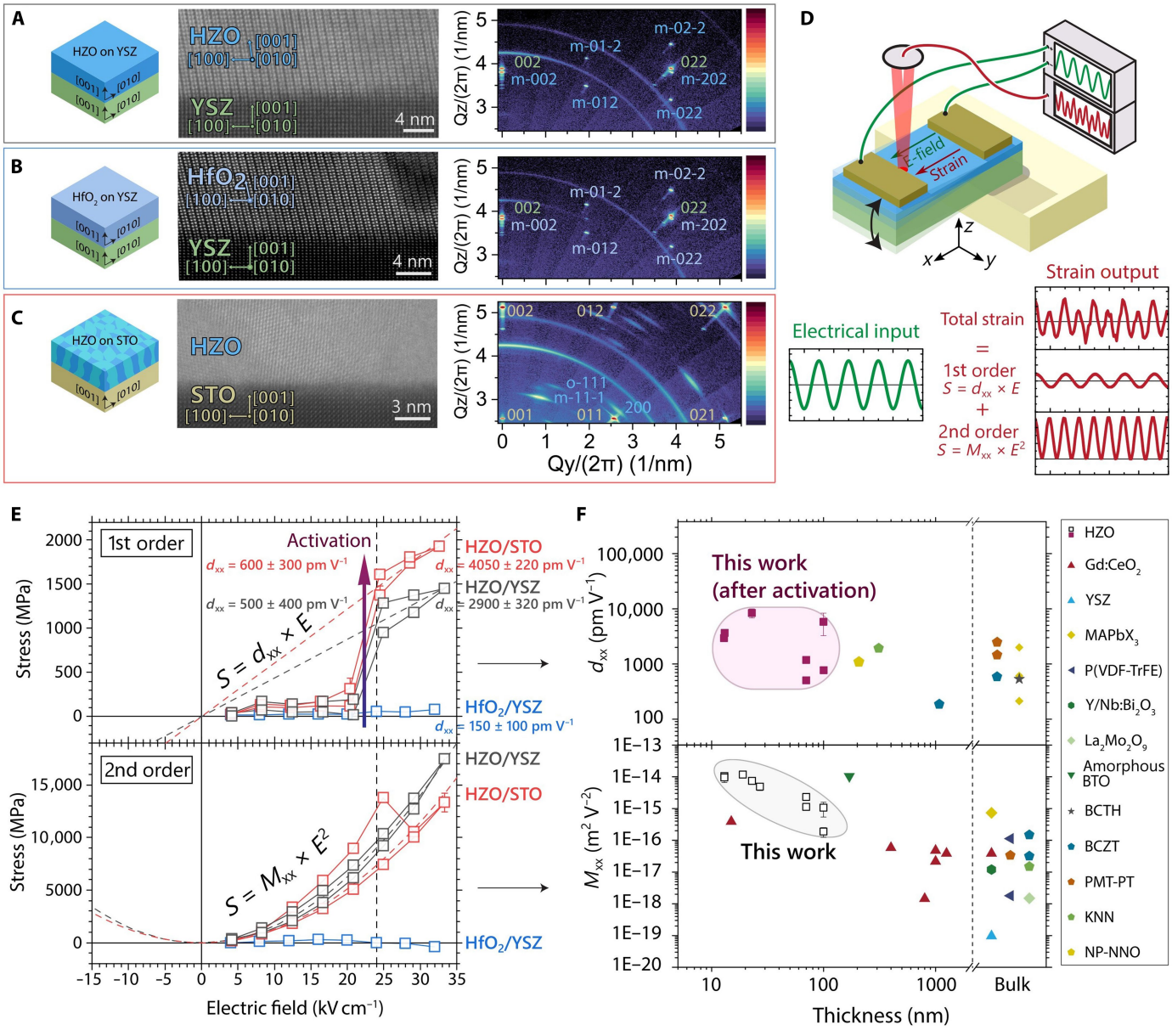


Fig. 1. System structure and electromechanical responses. (**A** to **C**) STEM HAADF cross-sectional images and reciprocal space maps of HZO/YSZ, HfO_2/YSZ, and HZO/STO samples, showing the crystalline structure of each sample: HZO/YSZ and HfO_2/YSZ are epitaxially matched to the YSZ substrate, and HZO/STO is textured polycrystalline; (**D**) experimental setup for interferometry measurements in the cantilever configuration and experimental strain measurement composed of first and second harmonics; (**E**) first- and second-order electromechanical response of each sample (10-nm thick) measured by interferometry; (**F**) comparison of the measured piezoelectric (d_{xx}) and electrostrictive (M_{xx}) coefficients with other notable electromechanically active single-layer materials. Data in (F) are taken from (*39*, *47*–*56*). [(C), right] reproduces the same RSM shown in fig. S1B (bottom right) for direct comparison.

differences observed in HZO films on STO, highlight the dominant role of chemical composition in determining functional performance. In contrast, film orientation appears to have a negligible effect on electromechanical behavior. Since the observed responses are not correlated with crystal phase or orientation but instead with composition, we examine the nanoscale structural characteristics of HZO and hafnia films on YSZ. Although both films display comparable structural features, only HZO demonstrates remarkable electromechanical activity. This suggests that defects such as grain boundaries, stacking faults, and elastic dipoles may modulate the response through their influence on phase transformation-driven mechanisms. A focused STEM analysis of HZO and hafnia films on YSZ was conducted to examine the effect of lattice strain on electrostrictive behavior. Analyses reported in fig. S4 highlight several structural features in the epitaxial thin films of HZO/YSZ and HfO_2/YSZ. Local distortions and stacking faults are present throughout the films to relax the lattice mismatch, while highly coherent grain boundaries arise from the preferred orientations. Moreover, we notice more dislocations and stacking faults in HZO films, although thicker samples show no clear difference in coherence or dislocation

Downloaded from https://www.science.org at Forschungszentrum Juelich Gmbh on November 19, 2026

density. Additional RSM and TEM analyses of strain reveal that maximal electrostriction occurs in films with a shrinkage of the monoclinic *c* axis by 0.35% and expansion of the *b* axis by 0.14%, concurring with a decrease in the monoclinic β angle from 99.5° to 99.15° (figs. S5 and S6). In this same line, synchrotron-based nano–x-ray diffraction (XRD) measurements were undertaken, aiming to resolve local distortions resulting from lattice tilting and strain. However, up to the maximum field applied (0.3 kV cm^{-1}), no substantial changes were observed, indicating no dominant individual distortion in this regime (figs. S7 and S8).

Overall, the analyses suggest that the samples' orientation and phase are not the main factors influencing the electromechanical behavior. Still, the presence of Zr is required to observe an electromechanical coupling in hafnia-based thin films. For further confirmation, we measured the electromechanical activity of structurally disordered (quasi-amorphous) samples obtained by lowering the deposition temperature to 50°C (see fig. S9). They show no first-order response, but a large second-order response, which is strong enough for the 30-nm thin film to break the 0.5-mm-thick substrate ($M_{xx} = 4 \times 10^{-15}$ m^2 V^{-2}) (fig. S9D). Since we see large electrostriction in disordered samples with no overall orientation, these results highlight that the crystal orientation does not affect the electrostriction of HZO. However, the appearance of the first-order response above the threshold field in ordered films suggests the existence of a phase transformation leading to the piezoelectric-like behavior of the samples. A sufficiently large electric field could activate the first-order response by a structural transformation to a polar phase.

Local electromechanical measurements

To elucidate the behavior at the nanoscale, we use piezoresponse force microscopy (PFM) in an in-plane geometry of the best-performing HZO/YSZ thin films (see Materials and Methods and fig. S10 for details). The measurements reveal that, while the film surface height varies slightly, the first flexural resonant frequency of the cantilever remains largely unaffected, with minor variations in the lateral PFM amplitude and phase signals (fig. S10). PFM imaging before dc biasing reveals a uniform distribution of the piezo response across the surface with no substantial variation (fig. S10). The sample becomes piezoelectrically active after applying a dc voltage, showing apparent domain contrast in the areas switched by the different polarities of the applied voltage (Fig. 2, A and B). Switching spectroscopy PFM (SS-PFM) measurements confirm a first-order electromechanical response, validating the electromechanical activation observed in lower-frequency measurements (Fig. 2C and fig. S10). The local switching experiments and SS-PFM hysteresis loops attest that the material proceeds through a nonpolar-to-polar transformation under the action of the electric field above a threshold value of 2 to 3 V, thus exhibiting induced piezoelectric-like behavior. The lower switching voltage arises from the distinct geometry of SS-PFM, where the voltage is localized at a nanoscale tip-to-sample contact, producing a much higher local field than the macroscopic electrode configuration used in interferometry. Moreover, SS-PFM operates at higher frequencies than our quasi-static electromechanical measurements, further affecting switching dynamics.

To obtain deeper insight into the variation of the best-performing HZO/YSZ samples' electromechanical signal, PFM measurements were performed using the scheme presented as an inset in Fig. 2D to match the interferometry measurements as closely as possible. A voltage was applied between the two electrodes, while the AFM probe acted as a sensor for surface deformation, replicating the interferometric scheme. The first- and second-order responses in Fig. 2 (D and E) show apparent linear and quadratic behavior and allow extracting the values of the effective piezoelectric and electrostriction coefficients measured by PFM: $d_{xx} = 0.5$ pm V^{-1} and $M_{xx} = 1.65 \times 10^{-17}$ m^2 V^{-2}, respectively. Both coefficients are notably lower than those measured using interferometry. This change is consistent with the experimental frequency dependence of the electromechanical response (Fig. 2, F and G), since in PFM, measurements are performed at high frequencies, around 300 kHz. By fitting the experimentally measured deflection to finite-element simulations of the cantilever's displacement, numerical predictions of M_{xx} were made, which agree with the results in Fig. 2G (see fig. S11). Fluctuations in the response are observed near 50 and 1000 Hz in Fig. 2F and near 1000 Hz in Fig. 2G. The fluctuations near 50 Hz are due to environmental and mains noise affecting the first harmonic measurements, whereas the 1000-Hz fluctuations are caused by resonances in the cantilever system. The finite-element simulations (fig. S11) are fitted to the experimental data and are thus not revealing causalities.

Modeling and observation of the electrostrictive strain-driven phase transition

Density functional theory (DFT) simulations shed light on HfO_2 and HZO's phase stability under applied strain. We impose an artificial tensile uniaxial strain of up to 10% in the (100), (010), and (001) directions of the nonpolar monoclinic ($P2_1/c$), polar orthorhombic ($Pca2_1$), and antipolar orthorhombic (*Pbca*) phases of HZO and pure HfO_2 (schematics of these phases are shown in fig. S12). The most energetically stable phase under the applied strain is assessed upon relaxation of the structure. The results presented in Fig. 3 (A and B) (and fig. S13 for a comparison with the tetragonal $P4_2/nmc$ phase) show that after the initial stabilization of the phases at 2% strain, the energy per atom of each phase increases with increasing strain in each direction. However, an inversion of the stable phase occurs above 6% strain along the (010) direction of HfO_2 and HZO, where the polar orthorhombic phase becomes the most stable (*58*).

The transition into the polar orthorhombic phase is further corroborated by calculating the spontaneous polarization of uniaxially strained hafnia and HZO along the (010) direction. As shown in Fig. 3C, the $Pca2_1$ phase exhibits spontaneous polarization values of 51.79 and 52.42 μC/cm^2 for the HfO2 and HZO structures in the [001] direction. These values are within a 5% error margin of those reported in the literature (*29*, *59*). Beyond 6% strain, a discontinuity appears in both the energy-strain curve and polarization values. This discontinuity arises from microstructural rearrangements in the local coordination environment of the Hf/Zr cations along the direction of the Pca21 polymorph. As illustrated in fig. S14, when a critical Hf/Zr-O interatomic distance, $\mathbf{d} \geq 2.36$ Å, is exceeded under strain, the metal coordination transitions from sevenfold to sixfold.

This reduction signifies a departure from the canonical $Pca2_1$ ferroelectric phase, which features sevenfold cation coordination, where each cation is surrounded by seven oxygen atoms, including three polar (threefold-coordinated) and four buffer (fourfold-coordinated) oxygens (*58*). These two oxygen sublattices, as described by Dutta *et al.* (*29*), are labeled O_I and O_{II} in fig. S14, with the O_I sublattice responsible for the polarization in the structure. The reduction in coordination disrupts this characteristic motif and stabilizes a new energy minimum that becomes more favorable than competing phases, leading to a sharp increase in calculated polarization values. In addition,

Downloaded from https://www.science.org at Forschungszentrum Juelich Gmbh on November 19, 2026

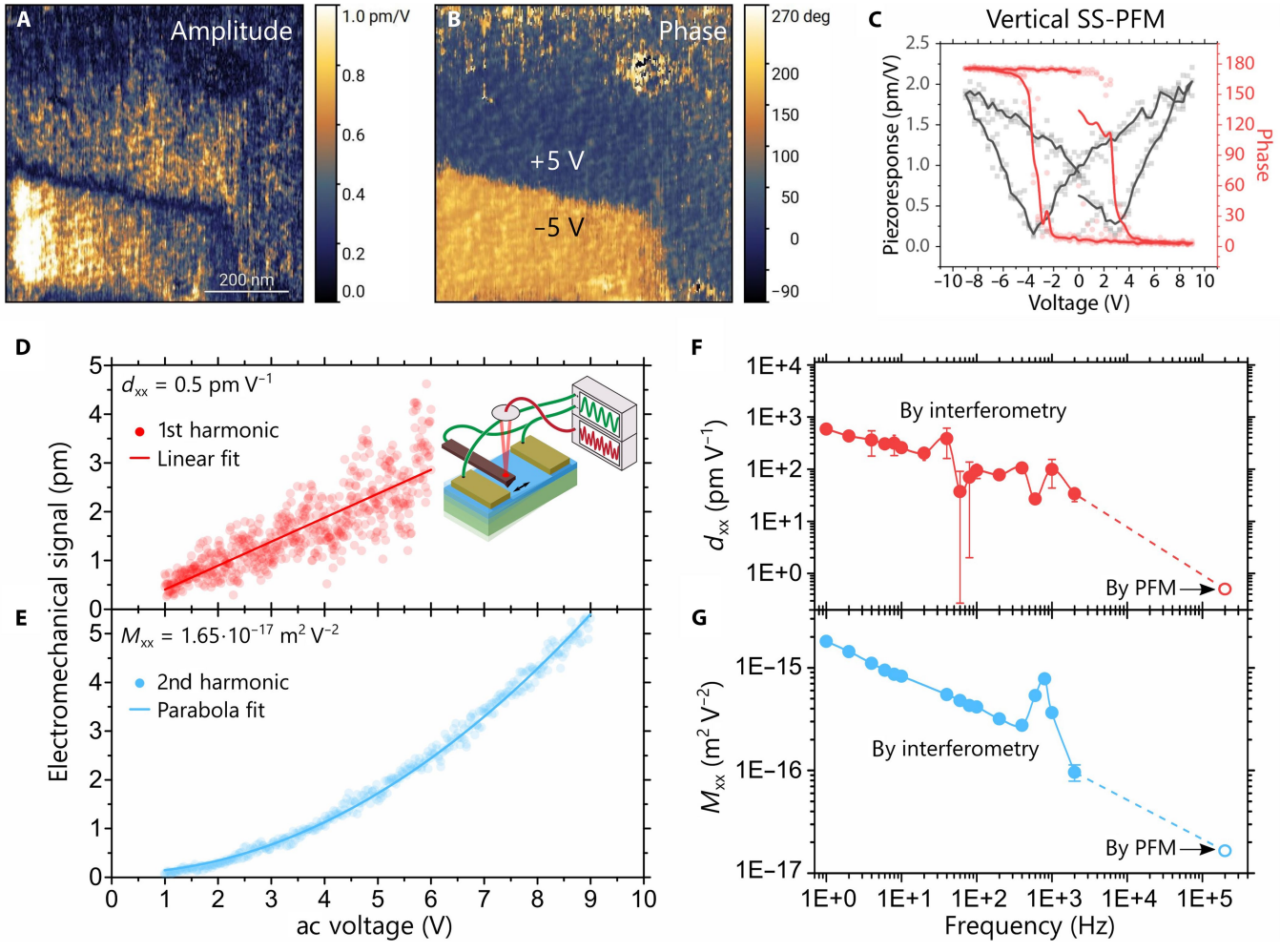


Fig. 2. Local electromechanical measurements using PFM with an in-plane geometry. (**A**) PFM amplitude and (**B**) PFM phase images after dc voltage application. (**C**) Average of five SS-PFM hysteresis loops. PFM voltage dependency measurements of the (**D**) first- and (**E**) second-order electromechanical response; inset schematic of the measurement and voltage application setup. Frequency dependence of (**F**) the effective piezoelectric and (**G**) the electrostrictive coefficients measured by interferometry and by PFM.

this coordination transition is specific to the strain direction; no similar changes in coordination geometry are observed among the other crystallographic directions examined. These findings demonstrate that high epitaxial strain can surpass energy barriers between different structural polymorphs and stabilize polar configurations that differ from the traditional sevenfold coordinated $Pca2_1$ phase.

Figure 3 (D and E) illustrates the crystal structures of the unstrained nonpolar monoclinic $P2_1/c$ phase and the uniaxially (010) strained polar orthorhombic $Pca2_1$ structure, with arrows highlighting the transformation from a nonpolar to a [001]-polarized structure. A notable subnanostructural change that triggers the phase transition is the decrease in average bond lengths, which reduces from 2.14 and 2.17 Å for monoclinic HfO_2 and HZO to 2.11 and 2.12 Å for orthorhombic HfO_2 and HZO, respectively (fig. S15). This finding also aligns with our RSM results (fig. S6) that maximum electrostriction occurs in films with a 0.4% shrinkage of the monoclinic *c* axis and a 0.2% expansion of the *b* axis. Moreover, the decrease in interatomic distances is accompanied by charge redistribution as the Hf/Zr coordination environment transitions from sevenfold to sixfold. This structural reorganization realigns the charge centers around the metal cations, inducing a net increase in polarization, as presented in Fig. 3F.

Following the DFT predictions, we performed in situ XRD measurements, tracking the position of the film and substrate Bragg peaks. At the same time, a dc electric field is applied to the electrodes along HZO's (010) axis (Fig. 3G), as confirmed by our TEM measurements. In this way, any lattice change caused by the applied field is observed as a shift of the Bragg peak position. However, numerous HZO (200) peaks appear for 2θ values between 34.0° and 35.3° (*59*), making it difficult to distinguish between the phases due to their proximity. Nevertheless, the observed shift (Δd) toward lower angles in fig. S16 suggests a phase transition from the monoclinic to the orthorhombic structure. Figure 3H displays the results for HZO and hafnia deposited on YSZ and a bare YSZ substrate for reference. Hafnia on YSZ and the bare substrate do not show any substantial change in peak position with increasing electric field, confirming our previous observations. On the other hand, the HZO/YSZ sample shows a change in both the HZO and YSZ peak positions, indicating a change in the

Downloaded from https://www.science.org at Forschungszentrum Juelich Gmbh on November 19, 2026

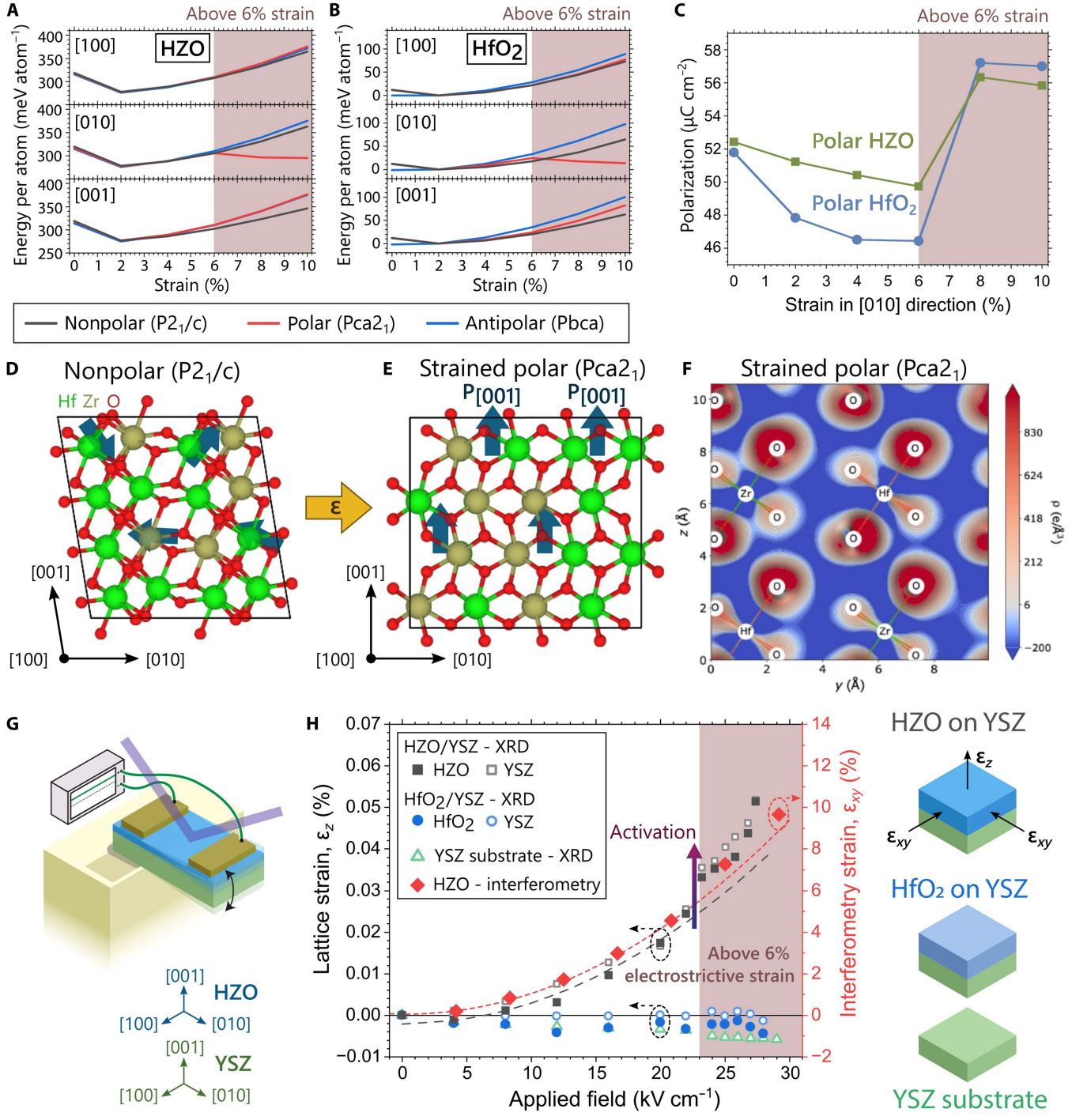


Fig. 3. Electrostrictive strain-driven phase transition. Calculations of the phase stability of (**A**) HZO and (**B**) HfO_2 under a uniaxial strain along the crystal's [100], [010], and [001] axes; (**C**) spontaneous polarization for the $Pca2_1$ HfO_2 and HZO structures strained along the [010] axis; crystal structures of (**D**) unstrained nonpolar monoclinic HZO Pbca and (**E**) (100)-oriented strained polar orthorhombic HZO $Pca2_1$, arrows indicate the transformation from a nonpolar to a [001]-polarized structure; (**F**) contour map of the charge density difference in (010)-oriented strained HZO $Pca2_1$. (**G**) Schematic of the in situ XRD measurement including crystalline orientations of HZO (blue) and YSZ (green). (**H**) First-order response activation—lattice strain calculated from Bragg peak position during in situ XRD measurements and laser interferometry, both measurements show a parabolic displacement and a stepwise increase in strain at 24 kV cm^{-1}.

Downloaded from https://www.science.org at Forschungszentrum Juelich Gmbh on November 19, 2026

atomic spacing. Moreover, the lattice strain in Fig. 3H shows the same trend of concurrent first- and second-order strain behavior as is seen in interferometry measurements, suggesting that the lattice strain observed by in situ XRD is linked to the electromechanical coupling. The observed shift in HZO and YSZ Bragg peaks can be ascribed to the YSZ substrate's lattice being strained by the HZO films under the electric field. Up to a dc electric field of 24 kV cm^{-1}, the HZO and YSZ peaks show a quadratic lattice strain, corresponding to $M_{xx} = 4.1 \times 10^{-17}$ m^2 V^{-2}. Once the in situ dc bias reaches 24 kV cm^{-1}, the lattice strain rises sharply by ~10%, following the same trend as the interferometry measurements done under ac fields (Fig. 3H). Both measurements show the combination of the electrostrictive displacement and a stepwise activation of the piezo-like strain at 24 kV cm^{-1}, suggesting a phase transition. Furthermore, the strains measured by XRD are in the same order of magnitude as those observed by PFM measurements. This suggests that device-scale effects other than the nanoscale lattice effects detected by XRD may be involved in the electromechanical response. Additional in situ XRD measurements of the 002 and 204 reflections under bias (0 → 500 → 725 → 0 V) demonstrate a fully reversible structural response, independent of electrode polarity. Two-axis XRD mapping further quantifies a reversible in-plane strain of ~−0.10% and an out-of-plane strain of ~+0.03%, confirming that the lattice distortion is elastic and reproducible rather than indicative of an irreversible phase change (fig. S16).

The in situ XRD, interferometry measurements, and DFT simulations imply that the activation of the first-order response is linked to a strain-induced phase transition from the nonpolar monoclinic to the polar orthorhombic phase caused by the large electrostrictive strain. Results in Fig. 3H confirm that we reach 6% electrostrictive strain at ~24 kV cm^{-1}, the same electric field value at which we observe both activation of the first-order response using interferometry and a step increase in lattice strain by in situ XRD.

Linearized electrostriction

To further explore the electromechanical coupling, we impose a combined ac and dc external electric field. Under these conditions, the crystal charge symmetry is disturbed, and the strain response becomes linearized, demonstrating a behavior reminiscent of piezoelectricity yet fundamentally arising from electrostriction (*7*, *60*). The contributions from a combined dc bias and ac voltage follow the equations below

$$\varepsilon(t) \propto M_{ij}\{U_{ac} \cdot \cos(2\pi ft) + U_{dc}\}^2 \quad (1)$$

$$\varepsilon(t) \propto 2M_{ij}U_{ac} \cdot U_{dc} \cdot \cos(2\pi ft) + M_{ij}\frac{U_{ac}^2}{2} \cdot \cos(2 \cdot 2\pi ft) + M_{ij} \cdot U_{dc}^2 \quad (2)$$

where $\varepsilon(t)$ is the strain response over time t at a frequency f, M_{ij} is the electrostriction coefficient, U_{ac} and U_{dc} are the external alternating electric field and bias. In Eq. 2, the first term describes the bias-induced first-order response, the second term is the classical second-order electrostrictive response, and the third term is proportional to U_{dc}^2 but does not change with time (*7*). Although comparable to the electromechanical response of piezoceramics, the bias-induced first-order response arises from the squared field dependency and the resulting cross-term combining ac field and dc bias. Nevertheless, such a response is a useful benchmark for comparing electrostrictive materials with piezoceramics (*61*), typically called pseudo-piezoelectricity (ϵ_{ij}), with values reported for both thin films and bulk ceramics (*7*, *8*, *60*, *61*).

The 5-Hz ac and dc signal superposition was applied to 10-nm films of HZO on YSZ and STO. For the applied ac and dc voltages, the linearized electrostriction contributes to a first-order response. Figure 4A presents stress dependence in HZO/YSZ and HZO/STO films as a function of combining dc and ac field ($U_{dc} \times U_{ac}$). The observed trend indicates the strong correlation between applied fields and the induced mechanical response, and both systems exhibit enhanced stress generation. More details can be found in fig. S17 (A and B). This further validates the linearization of the electrostriction, demonstrating the potential for tunable stress engineering via electric field modulation.

To quantify the linearized electrostrictive response, we extracted the pseudo-piezoelectric coefficient from the change in measured stress for the applied ac voltage, with a linear fit to the data presented in Fig. 4B. Here, ϵ_{xx} exceeds the highest previously reported value for Gd-doped CeO_2 (Fig. 4C) (*43*), further confirming the exceptional electromechanical performance of our system. In addition, the ϵ_{xx} values under dc bias reach values similar to the d_{zz} after activation (Fig. 4C), suggesting that the observed activation effect may be explained by the appearance of an internal dc bias in the system above a threshold electric field (i.e., due to polarization). Last, we extract the electrostriction coefficient M (fig. S17C) from the data shown in Fig. 4A by analyzing the total strain response using $M = \frac{\varepsilon}{2U_{ac}U_{dc}}$. The values obtained by linearization of the electrostriction agree with those found by analysis of the second-order strain response and confirm the values of $M_{xx} = 1 \times 10^{-14}$ m^2 V^{-2}, surpassing the highest reported values in the literature (*43*). Notably, mechanical failure of some samples is observed during electrical measurements, due to intense stress accumulation in the region between electrodes. Macroscopic cracks formed along the crystallographic cleavage planes of the substrate are documented using optical and electron microscopy (fig. S18).

DISCUSSION

Our findings uncover a previously unrecognized electromechanical regime in hafnium zirconium oxide (HZO), where field-driven instability of fluorite-derived phases gives rise to an extraordinary and tunable response. At low field amplitudes, HZO remains in its centrosymmetric monoclinic ground state, exhibiting a purely quadratic strain-field relationship with an electrostriction coefficient of $M = 1 \times 10^{-14}$ m^2 V^{-2}, the highest measured in a single-layer oxide. However, beyond a critical threshold of 24 kV cm^{-1}, the material undergoes a reversible phase transformation to a polar orthorhombic structure, activating an extrinsic piezoelectric-like response with effective coefficients exceeding 10,000 pm V^{-1}. The activation of the first-order response does not originate from intrinsic ferroelectricity or defect migration but rather from stabilization of the polar phase under large electrostrictive strain. The associated polarization introduces an internal bias, which effectively linearizes the second-order response into an amplified first-order response.

Although P-E and dielectric measurements could provide additional insight into the monoclinic-to-polar orthorhombic transition, the electric fields demanded by our sample configuration are prohibitively large and prevent stable testing. Adapting this study to conventional capacitive architectures offers a valuable path for future

Downloaded from https://www.science.org at Forschungszentrum Juelich Gmbh on November 19, 2026

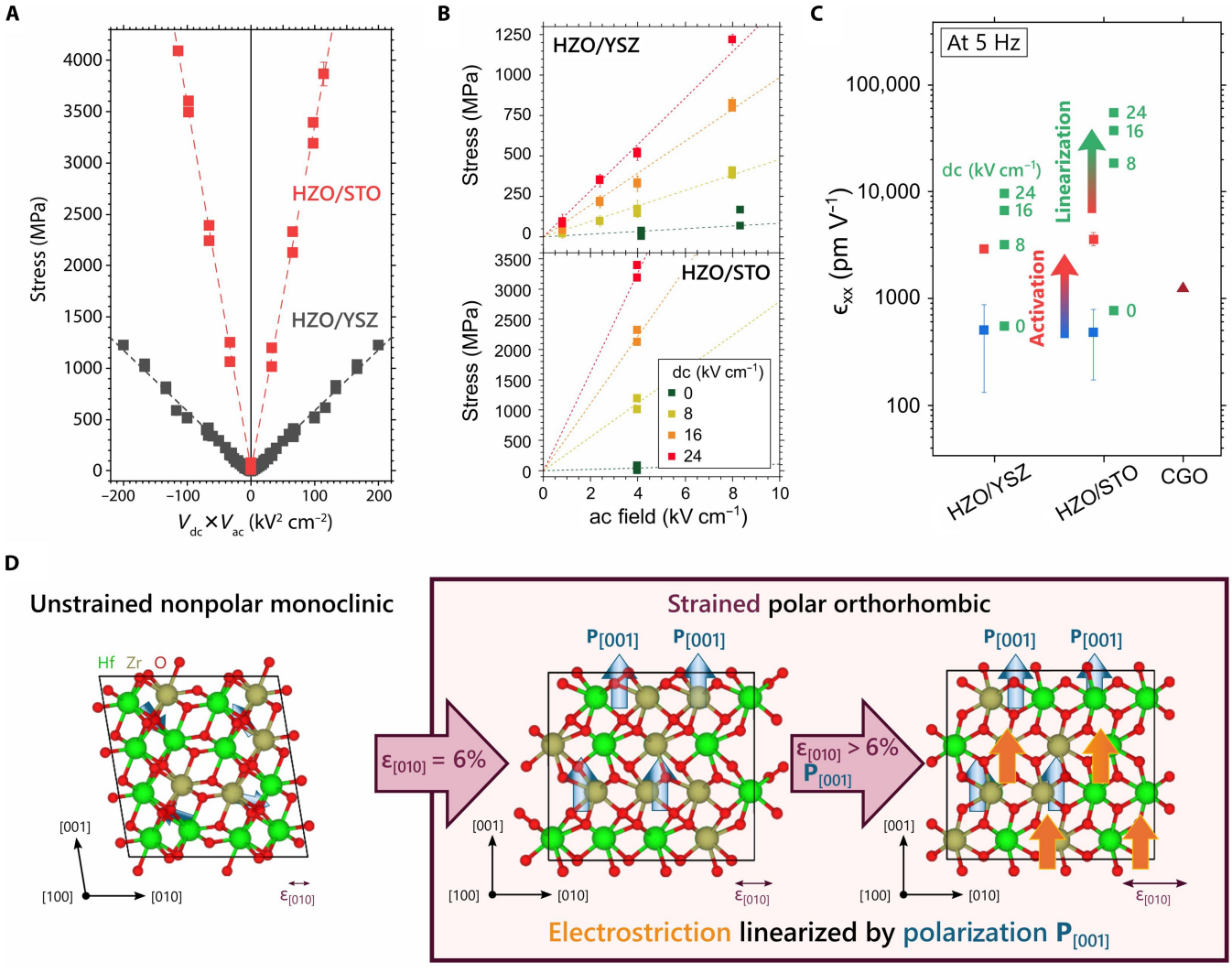


Fig. 4. Linearization of electrostriction by combining ac and dc electric fields. (**A**) Stress plotted against $V_{dc} \times V_{ac}$, showing linearization of the electrostriction. (**B**) Measured stress with increasing dc bias for different ac fields for HZO/YSZ and HZO/STO. (**C**) Calculated pseudo-*d* for each biasing level compared to *d* values before and after activation without bias. (**D**) Proposed mechanism for the observed effects: Nonpolar monoclinic HZO shows large electrostriction, when the electrostriction causes an electromechanical strain above 6%, monoclinic HZO transforms to polar orthorhombic HZO, the polarization causes internal dc biases to linearize the large electrostriction, and an extraordinarily large linear electromechanical strain is observed.

investigation, but these structures would inherently suppress the shear displacements central to the observed electromechanical response.

The electromechanical response of HZO is strongest under quasi-static and low-frequency excitation, which distinguishes it from conventional thin-film piezoelectrics designed for megahertz-gigahertz operation. Although this limits radio frequency applications, the colossal effective coefficients (>10,000 pm V^{-1}) reveal an electrostriction-driven phase instability that is scientifically important. Similar low-frequency giant responses have recently been highlighted in doped ceria (*43*), oxygen-deficient fluorites (*7*), and $NaNbO_3$ films with antiferroelectric-ferroelectric competition (*62*). These studies demonstrate that this behavior is valued as both a novel design approach and a benchmark for functional oxides. Beyond scientific insight, large displacements at low or intermediate frequencies are directly relevant for applications such as acoustofluidics (*63*), micropositioners, tunable optics, adaptive mechanics, and energy harvesting, where bandwidth is less critical.

Critically, this work introduces a design principle for electromechanical materials: leveraging field-induced symmetry breaking to access extreme responses in otherwise nonpiezoelectric systems. The ability to activate and control piezoelectricity extrinsically in a CMOS-compatible oxide positions HZO as a foundational material for next-generation actuators, sensors, and strain-adaptive nanoelectronics.

MATERIALS AND METHODS

Sample preparation

Thin films of undoped HfO_2 and HZO were grown onto crystals of (100)-oriented YSZ and STO by pulsed laser deposition using a COMPex-Pro KrF excimer laser with a wavelength of 248 nm and a

Downloaded from https://www.science.org at Forschungszentrum Juelich Gmbh on November 19, 2026

pulse duration of 20 to 30 ns. The laser fluence used was 1.3 J cm^{-2}, and the depositions were done in 0.1 mbar of oxygen at 800°C. The samples were cooled at a rate of 2°C min^{-1} in 0.1 mbar of oxygen. Film thicknesses were monitored by controlling the growth rate and then confirmed by measuring Laue oscillations in XRD measurements.

Gold electrodes (100-nm thickness) separated by 250 μm were sputtered on the films through a shadow mask to create contacts. The substrates were glued in a cantilever configuration onto glass slides, and copper wires were connected to the electrodes using silver paste (as shown in Fig. 1D).

X-ray diffraction

XRD and RSM measurements were done using a Rigaku Smartlab diffractometer. A Ge (200) 2-bounce monochromator was used to remove the $K_{\alpha 2}$ radiation line. XRD θ-2θ measurements were done using a zero-dimensional (0D) detector in Bragg-Brentano configuration. RSM measurements were done using a 2D detector to allow for fast scanning of large areas of reciprocal space.

In situ XRD measurements were done using a PANalytical X'Pert PRO diffractometer equipped with a Cu anode x-ray tube and a multichannel detector in Bragg-Brentano configuration. The measurements were carried out with the smallest divergence and antiscatter slits available (1/32° and 1/16°, respectively) and without monochromator to maximize intensity of the incident beam. The thin-film device was carefully positioned in the diffractometer in such manner so the incident beam would interact only with the 200-μm-wide region between the gold electrodes. Precise alignment was confirmed by the loss of the Au 111 peak in the diffraction pattern. During the measurement, the sample electrodes were connected to a Hamamatsu C4840 high-voltage power supply, and a static dc voltage was applied. Measurement parameters are as follows: 2θ range from 34.0490° to 35,4507°, step size of 0.0033°, 49,368-s counting time per step, the total measurement time was 5 min and 20 s, and an x-ray tube was operated at 40 kV and 30 mA. A schematic of the experimental setup is shown in Fig. 3G.

Scanning nano-XRD microscopy

The local microstructural evolution of HZO/YZS thin film was investigated in situ by electric field–induced changes in their (002) reflections via scanning nano-XRD under subcoercive electric fields (bipolar cycling up to ±15 V). The experiment was carried out at the NanoMAX beamline of MAX IV (Lund, Sweden) (*64*). A monochromatic 10-keV x-ray beam, at full flux mode (3×10^{10} photons/s), was focused to 88 nm by 88 nm using Kirkpatrick-Baez mirrors and scanned over a 2 μm–by–20 μm area with an exposure time of 0.1 s per step (~3 min per voltage step). An Eiger 500K 2D detector (75 μm × 75 μm pixel size) was placed 400 mm downstream of the sample in horizontal scattering geometry at 2θ = 28°. To minimize beam-induced damage, 2D-RSM was acquired at the peak of the rocking curve rather than through full 3D-RSM (fig. S19). The regions of interest (ROIs) in real space were identified by reconstructing the scattering signal from the Au electrodes in reciprocal space. After ROI localization, the structural parameters associated with strain, tilt, FWHM (full width at half maximum), and their associated spatial heterogeneity (i.e., SD) were averaged over the scanned area and evaluated as a function of the applied electric field (figs. S7 and S8).

Transmission electron microscopy

Cross-sectional liftouts for STEM analysis were taken using a Thermo Fisher Scientific Helios NanoLab 460F1 FIB-SEM, with a final milling energy of 2 kV. STEM HAADF imaging was done using two microscopes: a Hitachi High-Technologies HF5000 S/TEM and an FEI Titan G2 80-200 ChemiSTEM. TEM imaging and selected area diffraction were done using an FEI Titan 80-300 TEM. STEM imaging was done at 200 kV, and TEM imaging and diffraction were done at 300 kV. Mapping of the gradient of planar spacing was done using Hyperspy (*65*) and Atomap (*66*). Geometrical phase analysis on experimental images was performed using a DigitalMicrograph plugin (*67*).

Laser interferometry

We measure our samples in the cantilever configuration. One edge of the sample is fixed to a support, while the other edge is left overhanging and free to vibrate, as shown in fig. S20A. We use an AIM-TTI TGP 3100 function generator connected to a Trek 2220 amplifier to apply an oscillating electric field to samples. The electromechanical activity was measured with a single-beam laser interferometer SIOS NA analyzer. The laser spot was focused onto the top of the film, in the gap between the electrodes, to measure the displacement of the cantilever. An in-plane expansion of the film causes the cantilever tip to curve downward, whereas an in-plane compression of the film causes the cantilever tip to curve upward. The time and frequency components of the raw electromechanical signal are shown in fig. S20 (B and C). The amplitude of the oscillation at the chosen frequency was evaluated through an Ametek 7230 DSP 340 Lock-in Amplifier, by comparing the interferometry signal to the driving signal.

To remove any artifacts caused by the substrate reacting to the applied field, the displacement of the substrate crystal without any active layers is measured and subtracted from the displacement measured on the sample. The comparison between the samples and the bare YSZ and STO substrate crystals is shown in fig. S21.

The cantilever displacement is converted into the stress imparted to the cantilever by the film using Stoney formalism. If the thickness of the film h (10 to 100 nm) is negligible with respect to the thickness of the substrate H (500 μm), then the Stoney formula was then used to obtain the lateral stress σ from the vertical curvature κ of the cantilever

$$\sigma = \kappa \frac{Y_S H^2}{6h\left(1-\nu_S\right)} \tag{3}$$

where Y_S is the Young's modulus of the substrate, and ν_S is its Poisson ratio. The in-plane strain ε can further be obtained from the in-plane stress by using $\varepsilon = \frac{\sigma}{Y_F}$, where Y_F is the Young's modulus of the film. Since the in-plane electrodes only apply strain to the cantilever along one in-plane direction (M_{11}), κ can be obtained from the displacement d of the cantilever tip and the cantilever distance c on the substrate between the clamped and measurement points, using $\kappa = \frac{2d}{c^2}$. We therefore use the modified Stoney formula for nonuniform biaxial strain, as shown by Chidambaram *et al.* (*68*)

$$\sigma = \frac{d}{c^2} \frac{Y_S H^2}{3h\left(1-\nu_S\right)} \tag{4}$$

Downloaded from https://www.science.org at Forschungszentrum Juelich Gmbh on November 19, 2026

This formalism is widely accepted and has been used to characterize many thin films in cantilever configurations (*68*, *69*). We further confirm the measured cantilever displacements by modeling the system, as shown in fig. S11. The cantilever displacement is simulated using the finite-element method model introduced in our previous work (*60*) and briefly summarized below under computational details. By fitting to the measured displacement, a numerical value of the electrostrictive longitudinal coefficient M_{11} is obtained, consistent with experiments.

To assess potential Joule heating during voltage cycling, thermal images were captured before and after electrical stimulation using a FLIR C3x thermal camera. The sample consisted of a thin activation layer (10 to 100 nm) deposited on a single-crystal substrate (500-μm thick), with electrodes spaced 250 μm apart. Although the thermal camera's resolution can be affected by surface reflectivity, this approach allowed monitoring of possible temperature variations across the electrode gap. Thermal images are presented in the Supplementary Materials (fig. S22).

Maxwell strain is the strain caused by the Coulomb attraction between charged electrodes. The coefficient μ relating the Maxwell strain to the applied electric field can be calculated using $\mu = -\frac{1}{Y}\frac{\varepsilon_0\varepsilon_r}{2}$. The expected Maxwell strain for these samples was calculated, yielding a Maxwell strain coefficient value of $\mu = -1 \times 10^{-21}\ \mathrm{m^2\ V^{-2}}$, four orders of magnitude smaller than the smallest electrostriction coefficient we observe.

Piezoresponse force microscopy

PFM measurements and spectroscopy were carried out using an NTEGRA Aura scanning probe microscope (NT-MDT, the Netherlands) equipped with an external HFLI lock-in amplifier (Zurich Instruments, Switzerland) and an NI-6361 DAQ board (National Instruments Corp., USA). The measurements were performed at the first flexural contact resonance frequency using dual-frequency resonance tracking, with an ac voltage of 1 to 3 V applied to the probe per frequency bin. Platinum-coated Multi75-G probes (BudgetSensors, Bulgaria) were used for all measurements. These probes have a nominal tip radius of ~35 nm, a spring constant of ~5 N/m, and a typical contact resonance frequency of ~270 to 300 kHz.

Conventional vertical PFM measurements were conducted by applying a voltage to the probe while grounding the sample. Electrostriction measurements were performed by applying a voltage between surface electrodes, with the probe grounded and positioned between the electrodes to detect lateral surface displacement. All measurements were conducted in a controlled environment with relative humidity maintained below 5% by constant airflow in the microscope chamber.

SS-PFM was carried out using superimposed ac and dc voltages. The acquired data were processed using a custom Python code. The phase offset of the lock-in amplifier was adjusted to minimize the quadrature component of the hysteresis loop. Quantification of surface displacement was based on vertical and lateral force-distance curve measurements (*70*). A damped harmonic oscillator model was used to extract amplitudes, with additional normalization by the cantilever shape factor (*71*).

Computational details

Ab initio calculations were performed using the DFT framework in VASP (*72*, *73*). The exchange-correlation effects were addressed using the Perdew-Burke-Ernzerhof functional revised for solids (*74*) and by using projector-augmented wave (*75*)–based atomic pseudopotentials. Our calculations use a 520-eV energy cutoff to ensure proper convergence of the plane waves. The Γ-centered *k*-point grids were generated with a *k*-point density of 3 points/Å. The energy convergence criterion between consequent images was set to 1.0×10^{-7} eV, and the interatomic force criterion was set so that the norm of all the forces was lower than 0.05 eV/Å.

The pristine structures were extracted from the Materials Project database, and we allowed for the relaxation of atomic positions. The converged geometries were scaled to $2 \times 2 \times 2$ supercells. The HZO solid solutions are created with the ACAT (*76*) package that comes with the ASE software (*77*). Twenty-five different solid solutions were created for each of the three phases, and the top five most thermodynamically favored were allowed to proceed to the applied strain calculations together with the pristine supercells. PerQueue was used as the workflow manager for our calculations (*78*).

Three directions of uniaxial tensile strain, reaching up to 10% in increments of 2%, were analyzed parallel to the [100], [010], and [001] directions, while the orthogonal directions to the applied strain remained fixed. The resulting energies are compared against the ground state—the monoclinic phase. The calculations of spontaneous polarization were conducted in accordance with the modern theory of polarization (*79*). Crystal structure visualizations were made with the Visualization for Electronic and Structural Analysis software (*80*).

In the numerical model for the cantilever deflection, the independent fields are the mechanical displacement field $\boldsymbol{u}$ and the electric potential ϕ. The dependent fields are the strain tensor $\boldsymbol{s} = \frac{1}{2}\left[\nabla\boldsymbol{u} + (\nabla\boldsymbol{u})^{\mathrm{T}}\right]$, the electric field $\boldsymbol{E} = -\nabla\phi$, as well as the stress tensor σ and the electric displacement $\boldsymbol{D}$. In the experimental setup, a pure ac voltage $V = V^{\mathrm{ac}}\, e^{i\omega t}$ is applied to the electrodes of the electrostrictor so to leading order the electrostriction response takes the form

$$u_i = u_i^{(2)} e^{-\mathrm{i}2\omega t} + u_i^{(2)*} e^{\mathrm{i}2\omega t} \tag{5}$$

$$\phi = \phi^{(1)} e^{-\mathrm{i}\omega t} + \phi^{(1)*} e^{\mathrm{i}\omega t} \tag{6}$$

where the asterisk denotes complex conjugation. Because of the in-plane electrode placement, two simplifications are introduced in our model: (i) The electric Maxwell stress is negligible, leaving the electrostrictive response as the sole cause of the deflection, and (ii) the shear electrostrictive coefficient M_{31} is negligible, leaving the longitudinal coefficent M_{11} as the only electrostrictive coefficient in the model. This simplification combined with the assumption of isotropic materials results in the constitutive equations (using index notation) to second order in $\boldsymbol{u}$

$$\sigma_{ij} = C_{ijkl}(Y,\nu)\, s_{kl} + m_{ijkl}\left(Y,\nu,M_{11}\right) E_k E_l \tag{7}$$

$$D_i = \varepsilon_{ij}^{s}\, E_j, \text{with } i,j,k, \text{and } l \text{ being } x,y, \text{or } z \tag{8}$$

Here, Y is the Young's modulus, ν is the Poisson's ratio, M_{31} and M_{33} are respectively the shear and longitudinal electrostriction coefficients, ε_{ij}^{s} is the electric permittivity, δ_{ij} is the Kroenecker delta, and

Downloaded from https://www.science.org at Forschungszentrum Juelich Gmbh on November 19, 2026

the elastic moduli C_{ijkl} as well as the electromechanical coupling coefficients m_{ijkl} are given in terms of Y, ν, M_{11}, and M_{31}as described in the Supplementary Materials (eq. S2). The governing equations for $\boldsymbol{u}$ and ϕ are

$$\rho \partial_t^2 \boldsymbol{u} = \nabla \cdot \boldsymbol{\sigma}, 0 = \nabla \cdot \boldsymbol{D} \quad (9)$$

As in our previous work (*60*), we implement these equations in the Weak Form PDE Interface of COMSOL Multiphysics. The material's properties and geometrical parameters used in the simulations can be found in table S1 and fig. S23 in the Supplementary Materials. Using this longitudinal electrostriction model, we fit the simulated cantilever displacement to the measured displacement using the electrostriction coefficient M_{11} as the only fitting parameter. The dependence of M_{11} on frequency was derived using the method presented in our previous work (*60*) via a Taylor expansion of M_{11} in the deflection. Figure S11 shows how the simulated deflection versus frequency (open gray triangles and connecting curve) fits well the measured cantilever deflection (black squares). Also shown is the resulting fit of M_{11} versus frequency (blue points and connecting curve).

Supplementary Materials

This PDF file includes:

Figs. S1 to S23
Table S1
Supplementary Text

REFERENCES

1. P. Fedeli, F. Cuneo, L. Magagnin, L. Nobili, M. Kamlah, A. Frangi, On the simulation of the hysteresis loop of polycrystalline PZT thin films. *Smart Mater. Struct.* **29**, 095007 (2020).
2. T. Kobayashi, M. Ichiki, R. Kondou, K. Nakamura, R. Maeda, Degradation in the ferroelectric and piezoelectric properties of Pb(Zr,Ti)O_3 thin films derived from a MEMS microfabrication process. *J. Micromech. Microeng.* **17**, 1238–1244 (2007).
3. J. F. Scott, C. A. Paz De Araujo, Ferroelectric memories. *Science* **246**, 1400–1405 (1989).
4. T. Mikolajick, S. Slesazeck, H. Mulaosmanovic, M. H. Park, S. Fichtner, P. D. Lomenzo, M. Hoffmann, U. Schroeder, Next generation ferroelectric materials for semiconductor process integration and their applications. *J. Appl. Phys.* **129**, 100901 (2021).
5. B. Noheda, P. Nukala, M. Acuautla, Lessons from hafnium dioxide-based ferroelectrics. *Nat. Mater.* **22**, 562–569 (2023).
6. U. Schroeder, M. H. Park, T. Mikolajick, C. S. Hwang, The fundamentals and applications of ferroelectric HfO_2. *Nat. Rev. Mater.* **7**, 653–669 (2022).
7. V. B. Tinti, J. K. Han, V. Frederiksen, H. Chen, J. Wallentin, I. Kantor, A. Lyksborg-Andersen, T. W. Hansen, G. Bae, W. Song, E. Stamate, D. Z. de Florio, H. Bruus, V. Esposito, Oxygen-defective electrostrictors for soft electromechanics. *Sci. Adv.* **10**, eadq3444 (2024).
8. V. B. Tinti, A. Kabir, D. Zanetti de Florio, V. Esposito, "The role of dopant on the defect chemistry of metal oxides," in *Metal Oxide Defects: Fundamentals, Design, Development and Applications* (Elsevier, Amsterdam, 2023), pp. 313–353.
9. T. S. Böscke, J. Müller, D. Bräuhaus, U. Schröder, U. Böttger, Ferroelectricity in hafnium oxide thin films. *Appl. Phys. Lett.* **99**, 102903 (2011).
10. J. Müller, T. S. Böscke, U. Schröder, S. Mueller, D. Bräuhaus, U. Böttger, L. Frey, T. Mikolajick, Ferroelectricity in simple binary ZrO_2 and HfO_2. *Nano Lett.* **12**, 4318–4323 (2012).
11. D. Martin, J. Müller, T. Schenk, T. M. Arruda, A. Kumar, E. Strelcov, E. Yurchuk, S. Müller, D. Pohl, U. Schröder, S. V. Kalinin, T. Mikolajick, Ferroelectricity in Si-doped HfO_2 revealed: A binary lead-free ferroelectric. *Adv. Mater.* **26**, 8198–8202 (2014).
12. T. Nishimura, L. Xu, S. Shibayama, T. Yajima, S. Migita, A. Toriumi, Ferroelectricity of nondoped thin HfO_2 films in TiN/HfO_2/TiN stacks. *Jpn. J. Appl. Phys.* **55**, 08PB01 (2016).
13. J. Y. Park, D.-H. Choe, D. H. Lee, G. T. Yu, K. Yang, S. H. Kim, G. H. Park, S.-G. Nam, H. J. Lee, S. Jo, B. J. Kuh, D. Ha, Y. Kim, J. Heo, M. H. Park, Revival of ferroelectric memories based on emerging fluorite-structured ferroelectrics. *Adv. Mater.* **35**, 2204904 (2023).
14. K. H. Kim, I. Karpov, R. H. Olsson, D. Jariwala, Wurtzite and fluorite ferroelectric materials for electronic memory. *Nat. Nanotechnol.* **18**, 422–441 (2023).
15. J. Lyu, I. Fina, J. Fontcuberta, F. Sánchez, Epitaxial integration on Si(001) of ferroelectric $Hf_{0.5}Zr_{0.5}O_2$ capacitors with high retention and endurance. *ACS Appl. Mater. Interfaces* **11**, 6224–6229 (2019).
16. H. Y. Yoong, H. Wu, J. Zhao, H. Wang, R. Guo, J. Xiao, B. Zhang, P. Yang, S. J. Pennycook, N. Deng, X. Yan, J. Chen, Epitaxial ferroelectric $Hf_{0.5}Zr_{0.5}O_2$ thin films and their implementations in memristors for brain-inspired computing. *Adv. Funct. Mater.* **28**, 1806037 (2018).
17. M. Ghatge, G. Walters, T. Nishida, A 30-nm thick integrated hafnium zirconium oxide nano-electro-mechanical membrane resonator. *Appl. Phys. Lett.* **116**, 43501 (2020).
18. R. Materlik, C. Kunneth, A. Kersch, C. Künneth, A. Kersch, The origin of ferroelectricity in $Hf_{1-x}Zr_xO_2$: A computational investigation and a surface energy model. *J. Appl. Phys.* **117**, 134109 (2015).
19. M. Falkowski, A. Kersch, Optimizing the piezoelectric strain in ZrO_2- and HfO_2-based incipient ferroelectrics for thin-film applications: An ab initio dopant screening study. *ACS Appl. Mater. Interfaces* **12**, 32915–32924 (2020).
20. R. Batra, T. D. Huan, G. A. Rossetti Jr., R. Ramprasad, Dopants promoting ferroelectricity in hafnia: Insights from a comprehensive chemical space exploration. *Chem. Mater.* **29**, 9102–9109 (2017).
21. J. Müller, U. Schröder, T. S. Böscke, I. Müller, U. Böttger, L. Wilde, J. Sundqvist, M. Lemberger, P. Kücher, T. Mikolajick, L. Frey, Ferroelectricity in yttrium-doped hafnium oxide. *J. Appl. Phys.* **110**, 114113 (2011).
22. S. S. Fields, T. Cai, S. T. Jaszewski, A. Salanova, T. Mimura, H. H. Heinrich, M. David Henry, K. P. Kelley, B. W. Sheldon, J. F. Ihlefeld, S. S. Fields, S. T. Jaszewski, A. Salanova, T. Mimura, H. H. Heinrich, J. F. Ihlefeld, T. Cai, B. W. Sheldon, M. D. Henry, K. P. Kelley, Origin of ferroelectric phase stabilization via the clamping effect in ferroelectric hafnium zirconium oxide thin films. *Adv. Electron. Mater.* **8**, 2200601 (2022).
23. Y. Wei, P. Nukala, M. Salverda, S. Matzen, H. J. Zhao, J. Momand, A. S. Everhardt, G. Agnus, G. R. Blake, P. Lecoeur, B. J. Kooi, J. Íñiguez, B. Dkhil, B. Noheda, A rhombohedral ferroelectric phase in epitaxially strained $Hf_{0.5}Zr_{0.5}O_2$ thin films. *Nat. Mater.* **17**, 1095–1100 (2018).
24. S. Estandía, N. Dix, J. Gazquez, I. Fina, J. Lyu, M. F. Chisholm, J. Fontcuberta, F. Sánchez, Engineering ferroelectric Hf0.5Zr0.5O2 thin films by epitaxial stress. *ACS Appl. Electron. Mater.* **1**, 1449–1457 (2019).
25. S. Estandía, J. Gàzquez, M. Varela, N. Dix, M. Qian, R. Solanas, I. Fina, F. Sánchez, Critical effect of the bottom electrode on the ferroelectricity of epitaxial $HfZr_{0.5}O_2$ thin films. *J. Mater. Chem. C Mater.* **9**, 3486–3492 (2021).
26. M. Hoffmann, U. Schroeder, T. Schenk, T. Shimizu, H. Funakubo, O. Sakata, D. Pohl, M. Drescher, C. Adelmann, R. Materlik, A. Kersch, T. Mikolajick, Stabilizing the ferroelectric phase in doped hafnium oxide. *J. Appl. Phys.* **118**, 072006 (2015).
27. S. Zhou, J. Zhang, A. M. Rappe, Strain-induced antipolar phase in hafnia stabilizes robust thin-film ferroelectricity. *Sci. Adv.* **8**, 5953 (2022).
28. S. S. Cheema, D. Kwon, N. Shanker, R. dos Reis, S.-L. Hsu, J. Xiao, H. Zhang, R. Wagner, A. Datar, M. R. McCarter, C. R. Serrao, A. K. Yadav, G. Karbasian, C.-H. Hsu, A. J. Tan, L.-C. Wang, V. Thakare, X. Zhang, A. Mehta, E. Karapetrova, R. V. Chopdekar, P. Shafer, E. Arenholz, C. Hu, R. Proksch, R. Ramesh, J. Ciston, S. Salahuddin, Enhanced ferroelectricity in ultrathin films grown directly on silicon. *Nature* **580**, 478–482 (2020).
29. S. Dutta, P. Buragohain, S. Glinsek, C. Richter, H. Aramberri, H. Lu, U. Schroeder, E. Defay, A. Gruverman, J. Íñiguez, Piezoelectricity in hafnia. *Nat. Commun.* **12**, 7301 (2021).
30. H. Tan, T. Song, N. Dix, F. Sánchez, I. Fina, Vector piezoelectric response and ferroelectric domain formation in $Hf_{0.5}Zr_{0.5}O_2$ films. *J. Mater. Chem. C Mater.* **11**, 7219–7226 (2023).
31. A. Chouprik, S. Zakharchenko, M. Spiridonov, S. Zarubin, A. Chernikova, R. Kirtaev, P. Buragohain, A. Gruverman, A. Zenkevich, D. Negrov, Ferroelectricity in $Hf_{0.5}Zr_{0.5}O_2$ thin films: A microscopic study of the polarization switching phenomenon and field-induced phase transformations. *ACS Appl. Mater. Interfaces* **10**, 8818–8826 (2018).
32. K. P. Kelley, A. N. Morozovska, E. A. Eliseev, Y. Liu, S. S. Fields, S. T. Jaszewski, T. Mimura, S. Calderon, E. C. Dickey, J. F. Ihlefeld, S. V. Kalinin, Ferroelectricity in hafnia controlled via surface electrochemical state. *Nat. Mater.* **22**, 1144–1151 (2023).
33. E. Stylianidis, P. Surabhi, R. Hamming-Green, M. Salverda, Y. Wei, A. Burema, S. Matzen, T. Banerjee, A. Björling, B. Mukherjee, S. Dutta, H. Aramberri, J. Íñiguez, B. Noheda, D. Carbone, P. Nukala, Investigating the electromechanical behavior of unconventionally ferroelectric $Hf_{0.5}Zr_{0.5}O_2$-based capacitors through operando nanobeam x-ray diffraction. *Adv. Electron. Mater.* **9**, 2201298 (2023).
34. S. Kang, W.-S. Jang, A. N. Morozovska, O. Kwon, Y. Jin, Y.-H. Kim, H. Bae, C. Wang, S.-H. Yang, A. Belianinov, S. Randolph, E. A. Eliseev, L. Collins, Y. Park, S. Jo, M.-H. Jung, K.-J. Go, H. W. Cho, S.-Y. Choi, J. H. Jang, S. Kim, H. Y. Jeong, J. Lee, O. S. Ovchinnikova, J. Heo, S. V. Kalinin, Y.-M. Kim, Y. Kim, Highly enhanced ferroelectricity in HfO_2-based ferroelectric thin film by light ion bombardment. *Science* **376**, 731–738 (2022).
35. P. Nukala, M. Ahmadi, Y. Wei, S. de Graaf, E. Stylianidis, T. Chakrabortty, S. Matzen, H. W. Zandbergen, A. Björling, D. Mannix, D. Carbone, B. Kooi, B. Noheda, Reversible oxygen migration and phase transitions in hafnia-based ferroelectric devices. *Science* **372**, 630–635 (2021).
36. M. Pešić, F. P. G. Fengler, L. Larcher, A. Padovani, T. Schenk, E. D. Grimley, X. Sang, J. M. LeBeau, S. Slesazeck, U. Schroeder, T. Mikolajick, Physical mechanisms behind the field-cycling behavior of HfO_2-based ferroelectric capacitors. *Adv. Funct. Mater.* **26**, 4601–4612 (2016).

Downloaded from https://www.science.org at Forschungszentrum Juelich Gmbh on November 19, 2026

37. X. Li, Z. Liu, A. Gao, Q. Zhang, H. Zhong, F. Meng, T. Lin, S. Wang, D. Su, K. Jin, C. Ge, L. Gu, Ferroelastically protected reversible orthorhombic to monoclinic-like phase transition in ZrO_2 nanocrystals. *Nat. Mater.* **23**, 1057–1064 (2024).
38. S. Santucci, M. Vasiljevic, H. Zhang, V. B. Tinti, A. Bergne, A. A. Morin-Martinez, S. K. Chaluvadi, P. Orgiani, S. Sanna, A. Lyksborg-Andersen, T. W. Hansen, I. E. Castelli, N. Pryds, V. Esposito, Enhanced non-classical electrostriction in strained tetragonal ceria. *Nat. Commun.* **16**, 36 (2025).
39. H. Zhang, N. Pryds, D. S. Park, N. Gauquelin, S. Santucci, D. V. Christensen, D. Jannis, D. Chezganov, D. A. Rata, A. R. Insinga, I. E. Castelli, J. Verbeeck, I. Lubomirsky, P. Muralt, D. Damjanovic, V. Esposito, Atomically engineered interfaces yield extraordinary electrostriction. *Nature* **609**, 695–700 (2022).
40. H. Zhang, I. E. Castelli, S. Santucci, S. Sanna, N. Pryds, V. Esposito, Atomic-scale insights into electro-steric substitutional chemistry of cerium oxide. *Phys. Chem. Chem. Phys.* **22**, 21900–21908 (2020).
41. M. Varenik, B. Xu, J. Li, E. Gaver, E. Wachtel, D. Ehre, P. K. Routh, S. Khodorov, A. I. Frenkel, Y. Qi, I. Lubomirsky, Lead-free Zr-doped ceria ceramics with low permittivity displaying giant electrostriction. *Nat. Commun.* **14**, 43032 (2023).
42. T. Pechersky-Savich, B. Xu, M. Varenik, J. Li, E. Wachtel, D. Ehre, P. K. Routh, N. Marcella, A. I. Frenkel, Y. Qi, I. Lubomirsky, Correlated displacement of dynamic elastic dipoles produces nonclassical electrostriction in Zr-doped ceria. *Chem. Mater.* **36**, 7622–7634 (2024).
43. D. S. Park, M. Hadad, L. M. Riemer, R. Ignatans, D. Spirito, V. Esposito, V. Tileli, N. Gauquelin, D. Chezganov, D. Jannis, J. Verbeeck, S. Gorfman, N. Pryds, P. Muralt, D. Damjanovic, Induced giant piezoelectricity in centrosymmetric oxides. *Science* **375**, 653–657 (2022).
44. T. Shiraishi, T. J. Konno, H. Funakubo, Ferroelectric and piezoelectric properties of 100 nm-thick CeO_2-HfO_2 epitaxial films. *Appl. Phys. Lett.* **120**, 132901 (2022).
45. K. Katayama, T. Shimizu, O. Sakata, T. Shiraishi, S. Nakamura, T. Kiguchi, A. Akama, T. J. Konno, H. Uchida, H. Funakubo, Orientation control and domain structure analysis of {100}-oriented epitaxial ferroelectric orthorhombic HfO_2-based thin films. *J. Appl. Phys.* **119**, 134101 (2016).
46. I. Fina, F. Sánchez, Epitaxial ferroelectric HfO_2 films: Growth, properties, and devices. *ACS Appl. Electron. Mater.* **3**, 1530–1549 (2021).
47. S. K. Parate, S. Vura, S. Pal, U. Khandelwal, R. S. S. Ventrapragada, R. K. Rai, S. H. Molleti, V. Kumar, G. Patil, M. Jain, A. Mallya, M. Ahmadi, B. Kooi, S. Avasthi, R. Ranjan, S. Raghavan, S. Chandorkar, P. Nukala, Giant electrostriction-like response from defective non-ferroelectric epitaxial $BaTiO_3$ integrated on Si (100). *Nat. Commun.* **15**, 1428 (2024).
48. S. Santucci, H. Zhang, S. Sanna, N. Pryds, V. Esposito, Enhanced electro-mechanical coupling of TiN/$Ce_{0.8}Gd_{0.2}O_{1.9}$ thin film electrostrictor. *APL Mater.* **7**, 071104 (2019).
49. F. Li, D. Lin, Z. Chen, Z. Cheng, J. Wang, C. Li, Z. Xu, Q. Huang, X. Liao, L. Q. Chen, T. R. Shrout, S. Zhang, Ultrahigh piezoelectricity in ferroelectric ceramics by design. *Nat. Mater.* **17**, 349–354 (2018).
50. H. Liu, H. Wu, K. P. Ong, T. Yang, P. Yang, P. K. Das, X. Chi, Y. Zhang, C. Diao, W. K. A. Wong, E. P. Chew, Y. F. Chen, C. K. I. Tan, A. Rusydi, M. B. H. Breese, D. J. Singh, L. Q. Chen, S. J. Pennycook, K. Yao, Giant piezoelectricity in oxide thin films with nanopillar structure. *Science* **369**, 292–297 (2020).
51. M. Waqar, H. Wu, K. P. Ong, H. Liu, C. Li, P. Yang, W. Zang, W. H. Liew, C. Diao, S. Xi, D. J. Singh, Q. He, K. Yao, S. J. Pennycook, J. Wang, Origin of giant electric-field-induced strain in faulted alkali niobate films. *Nat. Commun.* **13**, 3176 (2022).
52. S. E. Park, T. R. Shrout, Ultrahigh strain and piezoelectric behavior in relaxor based ferroelectric single crystals. *J. Appl. Phys.* **82**, 1804–1811 (1997).
53. W. Liu, X. Ren, Large piezoelectric effect in Pb-free ceramics. *Phys. Rev. Lett.* **103**, 257602 (2009).
54. A. Piorra, V. Hrkac, N. Wolff, C. Zamponi, V. Duppel, J. Hadermann, L. Kienle, E. Quandt, $(Ba_{0.85}Ca_{0.15})(Ti_{0.9}Zr_{0.1})O_3$ thin films prepared by PLD: Relaxor properties and complex microstructure. *J. Appl. Phys.* **125**, 244103 (2019).
55. C. Zhao, W. Wu, H. Wang, J. Wu, Site engineering and polarization characteristics in $(Ba_{1-y}Ca_y)(Ti_{1-x}Hf_x)O_3$ lead-free ceramics. *J. Appl. Phys.* **119**, 24108 (2016).
56. M. Vasiljevic, M. Kollár, D. Spirito, L. Riemer, L. Forró, E. Horváth, S. Gorfman, D. Damjanovic, M. Vasiljevic, L. Riemer, D. Damjanovic, M. Kollár, E. Horváth, R. Aviv, T. Aviv, I. L. Forró, L. Forró, "Forbidden" polarisation and extraordinary piezoelectric effect in organometallic lead halide perovskites. *Adv. Funct. Mater.* **32**, 2204898 (2022).
57. E. D. Grimley, T. Schenk, X. Sang, M. Pešic, U. Schroeder, T. Mikolajick, J. M. LeBeau, E. D. Grimley, X. Sang, J. M. LeBeau, T. Schenk, M. Pešic, U. Schroeder, T. Mikolajick, Structural changes underlying field-cycling phenomena in ferroelectric HfO_2 thin films. *Adv. Electron. Mater.* **2**, 1600173 (2016).
58. T. Zhu, L. Ma, S. Deng, S. Liu, Progress in computational understanding of ferroelectric mechanisms in HfO_2. *npj Comput. Mater.* **10**, 122 (2024).
59. T. D. Huan, V. Sharma, G. A. Rossetti, R. Ramprasad, Pathways towards ferroelectricity in hafnia. *Phys. Rev. B* **90**, 064111 (2014).
60. V. B. Tinti, M. Vasiljevic, M. Grønborg, H. Chen, V. Frederiksen, I. Kantor, J. Wallentin, H. Bruus, V. Esposito, Electromechanical coupling in polaronic ceria. *J. Phys. Energy* **7**, 035002 (2025).
61. R. Korobko, E. Wachtel, I. Lubomirsky, Cantilever resonator based on the electrostriction effect in Gd-doped ceria. *Sens. Actuators A Phys.* **201**, 73–78 (2013).
62. B. Lin, K. P. Ong, T. Yang, Q. Zeng, H. K. Hui, Z. Ye, C. Sim, Z. Yen, P. Yang, Y. Dou, X. Li, X. Gao, C. K. I. Tan, Z. S. Lim, S. Zeng, T. Luo, J. Xu, X. Tong, P. W. F. Li, M. Ren, K. Zeng, C. Sun, S. Ramakrishna, M. B. H. Breese, C. Boothroyd, C. Lee, D. J. Singh, Y. M. Lam, H. Liu, Ultrahigh electromechanical response from competing ferroic orders. *Nature* **633**, 798–803 (2024).
63. C. Zhang, P. Brunet, S. Liu, X. Guo, L. Royon, X. Qin, X. Wei, Acoustofluidics at audible frequencies—A review. *Engineering* **44**, 51–72 (2025).
64. U. Johansson, D. Carbone, S. Kalbfleisch, A. Björling, M. Kahnt, S. Sala, T. Stankevic, M. Liebi, A. R. Fernandez, B. Bring, D. Paterson, K. Thanell, P. Bell, D. Erb, C. Weninger, Z. Matej, L. Roslund, K. Ahnberg, B. N. Jensen, H. Tarawneh, A. Mikkelsen, U. Vogt, NanoMAX: The hard x-ray nanoprobe beamline at the MAX IV Laboratory. *J. Synchrotron Radiat.* **28**, 1935–1947 (2021).
65. F. de la Peña, E. Prestat, J. Lähnemann, V. T. Fauske, P. Burdet, P. Jokubauskas, T. Furnival, C. Francis, M. Nord, T. Ostasevicius, K. E. MacArthur, D. N. Johnstone, M. Sarahan, J. Taillon, T. Aarholt, pquinn-dls, V. Migunov, A. Eljarrat, J. Caron, T. Nemoto, T. Poon, S. Mazzucco, sivborg, actions-user, N. Tappy, N. Cautaerts, S. Somnath, T. Slater, M. Walls, pietsjoh, hyperspy/hyperspy: v2.3.0. doi:10.5281/ZENODO.14956374 (2025).
66. M. Nord, P. E. Vullum, I. MacLaren, T. Tybell, R. Holmestad, Atomap: A new software tool for the automated analysis of atomic resolution images using two-dimensional Gaussian fitting. *Adv. Struct. Chem. Imaging* **3**, 9 (2017).
67. H. Du, GPA: Geometric Phase Analysis software. ResearchGate [Preprint] (2018). 10.13140/RG.2.2.26792.67845.
68. N. Chidambaram, D. Balma, R. Nigon, A. Mazzalai, R. Matloub, C. S. Sandu, P. Muralt, Converse mode piezoelectric coefficient for lead zirconate titanate thin film with interdigitated electrode. *J. Micromech. Microeng.* **25**, 045016 (2015).
69. R. Korobko, A. Patlolla, A. Kossoy, E. Wachtel, H. L. Tuller, A. I. Frenkel, I. Lubomirsky, Giant electrostriction in Gd-doped ceria. *Adv. Mater.* **24**, 5857–5861 (2012).
70. D. O. Alikin, L. V. Gimadeeva, A. V. Ankudinov, Q. Hu, V. Y. Shur, A. L. Kholkin, In-plane polarization contribution to the vertical piezoresponse force microscopy signal mediated by the cantilever "buckling". *Appl. Surf. Sci.* **543**, 148808 (2021).
71. N. Balke, S. Jesse, P. Yu, B. Carmichael, S. V. Kalinin, A. Tselev, Quantification of surface displacements and electromechanical phenomena via dynamic atomic force microscopy. *Nanotechnology* **27**, 425707 (2016).
72. G. Kresse, D. Joubert, From ultrasoft pseudopotentials to the projector augmented-wave method. *Phys. Rev. B* **59**, 1758 (1999).
73. G. Kresse, J. Furthmüller, Efficiency of ab-initio total energy calculations for metals and semiconductors using a plane-wave basis set. *Comput. Mater. Sci.* **6**, 15–50 (1996).
74. J. P. Perdew, A. Ruzsinszky, G. I. Csonka, O. A. Vydrov, G. E. Scuseria, L. A. Constantin, X. Zhou, K. Burke, Restoring the density-gradient expansion for exchange in solids and surfaces. *Phys. Rev. Lett.* **100**, 136406 (2008).
75. P. E. Blöchl, Projector augmented-wave method. *Phys. Rev. B* **50**, 17953 (1994).
76. S. Han, S. Lysgaard, T. Vegge, H. A. Hansen, Rapid mapping of alloy surface phase diagrams via Bayesian evolutionary multitasking. *npj Comput. Mater.* **9**, 1–14 (2023).
77. A. H. Larsen, J. J. Mortensen, J. Blomqvist, I. E. Castelli, R. Christensen, M. Dułak, J. Friis, M. N. Groves, B. Hammer, C. Hargus, E. D. Hermes, P. C. Jennings, P. B. Jensen, J. Kermode, J. R. Kitchin, E. L. Kolsbjerg, J. Kubal, K. Kaasbjerg, S. Lysgaard, J. B. Maronsson, T. Maxson, T. Olsen, L. Pastewka, A. Peterson, C. Rostgaard, J. Schiøtz, O. Schütt, M. Strange, K. S. Thygesen, T. Vegge, L. Vilhelmsen, M. Walter, Z. Zeng, K. W. Jacobsen, The atomic simulation environment—A Python library for working with atoms. *J. Phys. Condens. Matter* **29**, 273002 (2017).
78. B. H. Sjolin, W. S. Hansen, A. A. Morin-Martinez, M. H. Petersen, L. H. Rieger, T. Vegge, J. M. Garcia-Lastra, I. E. Castelli, PerQueue: Managing complex and dynamic workflows. *Digit. Discov.* **3**, 1832–1841 (2024).
79. N. A. Spaldin, A beginners guide to the modern theory of polarization. *J. Solid State Chem.* **195**, 2–10 (2012).
80. K. Momma, F. Izumi, VESTA 3 for three-dimensional visualization of crystal, volumetric and morphology data. *J. Appl. Cryst.* **44**, 1272–1276 (2011).

Acknowledgments

Funding: A.B., V.E., D.V.C., and N.P. acknowledge the Danish Council for Independent Research Technology and Production Sciences for the DFF Research Project 3 PILOT (grant no. 00069B). N.P. acknowledges the support from the ERC Advanced grant (NEXUS, 101054572), the research grant (VIL73726) from Villum Fonden, and the Danish Council for Independent Research Technology and Production Sciences for the DFF- Research Project 3 PILOT (grant no. 00069B). V.E., A.A.M.-M., and I.E.C. acknowledge the support from the Independent Research Fund Denmark under the grant "Nano-engineered solid state ionic metal oxides for near-room temperature oxygen conductivity" (NEMO) (grant no. 1032-00261B). A.A.M.-M. and I.E.C. also acknowledge support from the Novo Nordisk Foundation Data Science Research Infrastructure 2022 Grant: A high-performance computing infrastructure for data-driven research on sustainable energy materials, grant no. NNF22OC0078009. R.I. acknowledges the financial support from Latvian Council of Science under the grant "New generation of piezoelectric materials for active vibration

Downloaded from https://www.science.org at Forschungszentrum Juelich Gmbh on November 19, 2026

control" (grant no. LZP-2023/1-0571). A.K. and R.I. thank the ERA-Chair project "Felow-D" ("Low dimensional ferroelectrics for advanced electronic and biomedical application") funded by the European Union's Horizon 2020 research and innovation program under grant agreement number 101186499. R.I. acknowledges the support of Latvijas Zinatnes Padome LZP-2023/1-0571. M.V., D.A., A.K., and V.E. acknowledge the support from the Horizon Europe Framework Programme (HORIZON-TMA-MSCA-SE), project no. 101131229, Piezoelectricity in 2D materials: materials, modeling, and applications (PIEZO 2D). Part of this work (D.A. and A.K.) was developed within the scope of the project CICECO-Aveiro Institute of Materials, UIDB/50011/2020 (DOI 10.54499/UIDB/50011/2020), UIDP/50011/2020 (DOI 10.54499/UIDP/50011/2020), and LA/P/0006/2020 (DOI 10.54499/LA/P/0006/2020), financed by national funds through the FCT/MCTES (PIDDAC). D.A. acknowledges individual support by the 2023.09305.CEECIND/CP2840/CT0020 through contract (doi:10.54499/2023.09305.CEECIND/CP2840/CT0020) through national funds provided by FCT—Fundação para a Ciência e a Tecnologia. We acknowledge the MAX IV Laboratory for beamtime on the NanoMAX beamline under proposal 20240449. Research conducted at MAX IV, a Swedish national user facility, is supported by Vetenskapsrådet (Swedish Research Council, VR) under contract 2018-07152, Vinnova (Swedish Governmental Agency for Innovation Systems) under contract 2018-04969, and Formas under contract 2019-02496. J.W. acknowledges funding from the European Research Council (ERC) under the European Union's Horizon 2020 research and innovation program (grant 801847). Additional funding was provided by the Olle Engkvist Foundation, the Essence project, and the Swedish Research Council (contract no. 2021-04273). D.V.C. acknowledges the support from the Independent Research Fund Denmark for the Sapere Aude project Solid grant 10.46540/3123-00034B and the support of Novo Nordisk Foundation NERD Programme: New Exploratory Research and Discovery, Superior Grant NNF21OC0068015. D.J. acknowledges the support of Hitachi High-Technologies, in providing access to the Hitachi HF5000 S/TEM used in this work. W.R. and D.J. acknowledge support from the Deutsche Forschungsgemeinschaft via the Emmy Noether Programme under contract no Rh 146/1-1. V.E. and N.P. acknowledge support from the European Union through the European Innovation Council (EIC) and the Horizon Europe research and innovation programme under grant agreement no. 101099787 (ACOUSOME–Acoustofluidic thin-film actuated chip for exosome separation from blood). W.R. acknowledges support from the Deutsche Forschungsgemeinschaft (DFG) through grant RH 146/1-1 (ENP) and the DFG Collaborative Research Group FLAIR (project B04). **Author contributions:** Conceptualization: A.B., N.P., W.R., D.A., and V.E. Methodology: A.B., M.O.L.H., J.W., M.G., H.B., L.O., A.A.M.-M., V.B.T., R.I., V.E., W.R., D.A., and I.E.C. Investigation: A.B., J.W., M.G., D.J., H.B., L.O., D.K., A.A.M.-M., V.B.T., R.I., V.E., H.C., and D.A. Visualization: A.B., D.J., L.O., D.K., A.A.M.-M., V.B.T., R.I., V.E., M.V., and D.A. Supervision: M.O.L.H., J.W., H.B., D.V.C., A.K., V.E., M.V., W.R., and I.E.C. Writing—original draft: A.B., L.O., A.A.M.-M., V.E., and M.V. Writing—review and editing: A.B., M.O.L.H., J.W., M.G., N.P., D.J., H.B., D.V.C., L.O., A.A.M.-M., V.B.T., R.I., A.K., V.E., J.Z.-G., M.V., W.R., D.A., and I.E.C. Resources: H.B., D.K., A.A.M.-M., V.E., W.R., and I.E.C. Funding acquisition: N.P., H.B., D.V.C., V.E., and W.R. Data curation: A.B., J.W., H.B., L.O., D.K., A.A.M.-M., V.B.T., V.E., and J.Z.-G. Validation: A.B., M.O.L.H., H.B., D.K., A.A.M.-M., V.B.T., R.I., V.E., J.Z.-G., M.V., and D.A. Formal analysis: D.J., L.O., D.K., A.A.M.-M., V.B.T., R.I., V.E., and D.A. Project administration: H.B., V.E., and W.R. Software: M.O.L.H., J.W., H.B., L.O., A.A.M.-M., and I.E.C. **Competing interests:** The authors declare that they have no competing interests. **Data, code, and materials availability:** All data and code needed to evaluate and reproduce the results in the paper are present in the paper and/or the Supplementary Materials. Additional data supporting this study have been deposited in the Technical University of Denmark (DTU) data repository and are publicly available at https://doi.org/10.11583/DTU.30508754. This study did not generate new materials.

Submitted 25 June 2025
Accepted 13 May 2026
Published 26 June 2026
10.1126/sciadv.aea0750

Downloaded from https://www.science.org at Forschungszentrum Juelich Gmbh on November 19, 2026

ScienceAdvances

Electrostriction-driven phase instability enables giant pseudo-piezoelectricity in $Hf_{0.5}Zr_{0.5}O_2$

Achilles Bergne, Milica Vasiljevic, Denis Alikin, Victor Buratto Tinti, Leonardo Oliveira, Megan O. Landberg Hill, Huaiyu Chen, Jesper Wallentin, Dylan Jennings, Wolfgang Rheinheimer, Henrik Bruus, Mathias Grønborg, Dimitrios Koukoulis, Armando Antonio Morin-Martinez, Javier Zamudio-García, Ivano Eligio Castelli, Reinis Ignat#ns, Andrei Kholkin, Dennis Valbjørn Christensen, Nini Pryds, and Vincenzo Esposito

Sci. Adv. **12** (26), eaea0750. DOI: 10.1126/sciadv.aea0750

View the article online
https://www.science.org/doi/10.1126/sciadv.aea0750
Permissions
https://www.science.org/help/reprints-and-permissions

Downloaded from https://www.science.org at Forschungszentrum Juelich Gmbh on November 19, 2026

Use of this article is subject to the Terms of service

Science Advances (ISSN 2375-2548) is published by the American Association for the Advancement of Science. 1200 New York Avenue NW, Washington, DC 20005. The title *Science Advances* is a registered trademark of AAAS.

Copyright © 2026 The Authors, some rights reserved; exclusive licensee American Association for the Advancement of Science. No claim to original U.S. Government Works. Distributed under a Creative Commons Attribution NonCommercial License 4.0 (CC BY-NC).